

Article

Comparative Study of Random Forest and Support Vector Machine for Land Cover Classification and Post-Wildfire Change Detection

Yan-Cheng Tan ¹, Lia Duarte ^{2,3} and Ana Cláudia Teodoro ^{2,3,*}

¹ Department of Geography, Faculty of Arts and Humanities, University of Porto, Via Panorâmica, 4150-564 Porto, Portugal; yanchenggis@gmail.com

² Department of Geosciences, Environment and Land Planning, Faculty of Sciences, University of Porto, Rua Campo Alegre, 4169-007 Porto, Portugal; liaduarte@fc.up.pt

³ Earth Sciences Institute (ICT), Faculty of Sciences, University of Porto, Rua Campo Alegre, 4169-007 Porto, Portugal

* Correspondence: amteodor@fc.up.pt

Abstract: The land use land cover (LULC) map is extensively employed for different purposes. Machine learning (ML) algorithms applied in remote sensing (RS) data have been proven effective in image classification, object detection, and semantic segmentation. Previous studies have shown that random forest (RF) and support vector machine (SVM) consistently achieve high accuracy for land classification. Considering the important role of Portugal's Serra da Estrela Natural Park (PNSE) in biodiversity and nature conservation at an international scale, the availability of timely data on the PNSE for emergency evaluation and periodic assessment is crucial. In this study, the application of RF and SVM classifiers, and object-based (OBIA) and pixel-based (PBI) approaches, with Sentinel-2A imagery was evaluated using Google Earth Engine (GEE) platform for the land cover classification of a burnt area in the PNSE. This aimed to detect the land cover change and closely observe the burnt area and vegetation recovery after the 2022 wildfire. The combination of RF and OBIA achieved the highest accuracy in all evaluation metrics. At the same time, a comparison with the Normalized Difference Vegetation Index (NDVI) map and Conjunctural Land Occupation Map (COSc) of 2023 year indicated that the SVM and PBI map resembled the maps better.

Keywords: machine learning; land cover classification; object-based image analysis; pixel-based image analysis; random forest; support vector machine



Citation: Tan, Y.-C.; Duarte, L.; Teodoro, A.C. Comparative Study of Random Forest and Support Vector Machine for Land Cover Classification and Post-Wildfire Change Detection. *Land* **2024**, *13*, 1878. <https://doi.org/10.3390/land13111878>

Academic Editors: Linda See, Dmitry Schepaschenko and Myroslava Lesiv

Received: 13 September 2024
Revised: 24 October 2024
Accepted: 6 November 2024
Published: 10 November 2024



Copyright: © 2024 by the authors. Licensee MDPI, Basel, Switzerland. This article is an open access article distributed under the terms and conditions of the Creative Commons Attribution (CC BY) license (<https://creativecommons.org/licenses/by/4.0/>).

1. Introduction

Post-wildfire land cover change affects the ecosystem dynamics, biodiversity system, and ecological processes [1–19]. According to the European Commission, land cover indicates “the visible surface of land on Earth (e.g., crops, grass, water, broad-leaved, forest or built-up area)” [20]. While land cover plays a key role in environmental conditions in multiple ways [21], detecting the land cover change during a wildfire is critical. It enables the authorities to develop prompt disaster management strategies to prevent fatalities caused by landslides and flash floods following a wildfire [22]. Furthermore, periodic assessments scrutinizing burnt area recovery and vegetation dynamics after a wildfire provide valuable information for land management and biodiversity recovery monitoring.

According to Copernicus, Portugal is one of the countries most vulnerable to wildfires in the European Union [23]. On average, more than 200 forest fires happened annually in Portugal from 2013 to 2022 [23]. Portugal experienced the worst drought in 2017 since 1931, which caused 408 wildfires and involved 563,532 ha of burnt area [24,25]. In 2022, the Serra da Estrela Natural Park (PNSE), the largest protected area in Portugal, experienced the most significant fire since 1975 [26], which involved a burnt area of 21,942 ha [27]. This

study focused on the major burnt area in a wildfire that started on 6 August 2022 and ended on 2 September 2022 in PNSE [27]. The fire spread beyond the PNSE to Estrela Geopark. As a recognized Biogenetic Reserve and Geopark [28], the impacts of the large burnt area after the 2022 wildfire in the PNSE are concerning. Close monitoring of post-wildfire burnt area recovery and vegetation dynamics to observe the ecosystem dynamics and plan for disaster management is imperative.

The open data on land use and land cover (LULC) in Portugal are publicly available in vector format at a scale of 1:25,000 for Land Use and Occupation Map (COS) and in raster format with 10 m pixels for Conjunctural Land Occupation Map (COSc) from the National Geographic Information System (SNIG) [29,30]. LULC maps are widely used by various stakeholders for research, analysis, planning, and monitoring purposes [31–33]. However, continuous assessment and regular scrutiny of the land cover change are not achievable even with the annual update of the COSc [29]. To address this challenge, machine learning (ML) algorithms integrated with remote sensing (RS) data have proven increasingly effective for land cover classification since the late 1990s [34]. These techniques have enabled more accurate image classification, object detection, and semantic segmentation [35–37], particularly for environmental monitoring [9–11,15,16,18,19], urban planning [17,38], disaster management [3–5], and more. Previous studies proved that integrating ML algorithms and RS data is more efficient in land cover classification and achieves higher accuracy [39,40] than conventional methods [34].

ML algorithms such as Support Vector Machines (SVM) and Random Forest (RF) have emerged as particularly effective for land cover classification when integrated with RS data, when compared to other ML and Deep Learning (DL) algorithms such as Artificial Neural Networks (ANNs), K-Nearest Neighbors (K-NN), decision trees (DTs), and boosted DTs [32,34,39–43]. RF adopts an ensemble learning method formed by bagging, boosting, and stacking processes [44]. The advantages of RF are that it is robust to outliers, accurate, and less overfitting [45]. However, the right hyperparameters are decisive in achieving a high accuracy [46]. Also, RF cannot forecast values other than the feature range of the training data [47]. SVM uses kernel functions to maximize the margin between classes through a support vector and find the best hyperplane (optimal line) to define the best decision boundary for accurate predictions [48]. SVM is effective for clear class separation, able to handle linear/nonlinear tasks, good for diverse land covers, and memory-efficient [49]. However, SVM can be computationally expensive and not suitable for large datasets [50]. Two common methods for LULC classification are Object-Based Image Analysis (OBIA) and Pixel-Based Image Analysis (PBIA) [38]. OBIA groups the neighboring pixels with similar spectral properties and contextual information into meaningful objects. OBIA is useful for object identification in addition to pixel labeling. The quality of the object segmentation determines the final classification. Edge-based, region-based, and superpixel algorithms are common for OBIA segmentation [51,52]. PBIA is a traditional RS image classification commonly used in supervised and unsupervised techniques. PBIA classifies individual pixels based on their spectral properties without considering the adjacent pixels. Minimum Distance, Maximum Likelihood, and Spectral Angle Mapping are common algorithms available in many Geographic Information Systems (GIS) software for PBIA approaches [52–54].

Based on the literature, ML algorithms combined with remote sensing data and GIS analysis have been applied for land cover classification in several regions. Still, no similar methodology has been applied in this specific study area. Considering the important role of the PNSE in biodiversity and nature conservation at an international scale, the availability of timely data on the PNSE for emergency evaluation and periodic assessment is crucial. Hence, this study aimed to identify the most appropriate LULC approach and classifier for land cover classification to address the challenges faced for emergency evaluation and continuous assessment in the study area while serving as a reference for other forest regions with similar ecological characteristics prone to wildfires.

This study was conducted with the following specific objectives: (i) identifying the best model for land cover classification for the study area employing the integration of LULC classification (OBIA/PBIA) with a classifier (RF/SVM) on Google Earth Engine (GEE); and (ii) detecting the land cover change between pre-wildfire 2022, post-wildfire 2022, and summer 2023.

If an adequate model can be determined for the land cover classification in the study area, it will enable authorities to develop prompt disaster management strategies to prevent fatalities caused by landslides and flash floods following a wildfire and regular scrutiny on burnt area recovery and vegetation dynamics. This provides valuable risk management, land management, and biodiversity recovery monitoring information.

2. Materials and Methods

2.1. Study Area

The PNSE is a protected natural park with the highest mountain range in the central East of Portugal mainland and the largest protected area in the nation. The PNSE spans 89,132.21 ha across 9 municipalities of Belmonte, Celorico da Beira, Covilhã, Fornos de Algodres, Gouveia, Guarda, Manteigas, Oliveira do Hospital, and Seia [55]. The largest point of the Central Cordillera is the Tower, with the highest point at a 1991 m altitude [28], where over half of the natural park is above 700 m (Figure 1).

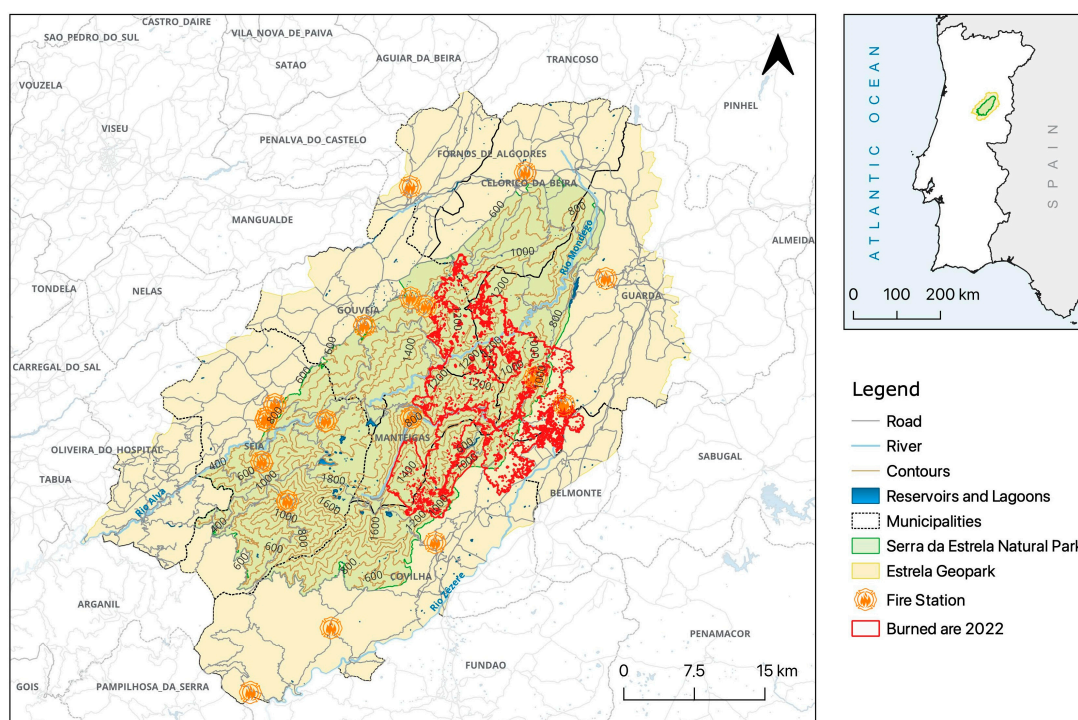


Figure 1. Serra da Estrela Natural Park. (Source: Fire Station from Google Earth, Road/River/Reservoirs and Lagoons from OSM, DEM from FCUP, PNSE boundaries from ICNF, Estrela Geopark/Municipalities from DGT, Spain from GADM; <https://www.geoparkestrela.pt/>, <https://zonacritica.pt/qestrela/>, accessed on 3 November 2023).

The PNSE's biodiversity thrives across 3 climate types—Mediterranean, Atlantic, and Continental—distributed over 3 altitudinal floors: basal, intermediate, and higher [28]. Its unique topography and climate foster exclusive species, subspecies, and varieties of flora and fauna. The PNSE mountain areas hide endemic species of flora and fauna, some of which only exist in this territory and nowhere else in the world, owing to its altitude and geographic isolation [28,55].

The PNSE was officially recognized as a Natural Park in July 1976, a Biogenetic Reserve in 1993, and a Natura 2000 Network in March 2008 [56,57]. In addition, the United Nations Educational, Scientific and Cultural Organization (UNESCO) recognizes the PNSE as a geopark, Estrela Geopark, for its remnants of the last glaciation, which occurred 30,000 years ago, and rocks aged up to 600 million years, which present high geodiversity [28]. Estrela Geopark, which occupies an area of 2216 km² surrounding the PNSE (Figure 1), boasts a diverse landscape that is evidence of multiple geological transformations, climatic contrasts, and ancient human settlement, with the first records dating back to the beginning of the 4th millennium B.C. This makes PNSE a territory of solid contrasts, where its tangible and intangible landscapes reflect a prolonged adaptation process and successive transformations. The rugged terrain makes it inhospitable for human occupation, which shapes the natural park biodiversity, and it is safe for a diversity of fauna and flora species [58]. Overall, the PNSE plays a crucial role in biodiversity and nature conservation on an international scale.

This study analyzed the land cover changes of the significant burnt area affected by the 2022 wildfire, which occurred from 6 August 2022 to 2 September 2022 in the PNSE [27]. The study area covers a burnt area beyond the PNSE to the Estrela Geopark (highlighted in red in Figure 1), which occupies 24,238.62 ha.

2.2. Data Sources

Sentinel 2A imagery (Level 2A) was used to measure the Difference Normalized Burn Ratio (dNBR) to identify the major burnt area in the PNSE post-wildfire 2022. Sentinel-2A imagery was acquired from ‘COPERNICUS/S2_SR_HARMONIZED’1 Image Collection using the *ee.ImageCollection* function on GEE [59]. Three images were selected by filtering the region of interest (ROI), relevant date range, and cloud coverage below 10% using *ee.ImageCollection.filterBounds()*, *ee.ImageCollection.filterDate()*, and *ee.Filter.metadata()* in GEE (Table 1) [60]. A buffer area around the major burnt area (Figure 1) was drawn as the ROI to include the neighboring spatial features, enhancing accuracy for the OBIA approach. Images before and after the 2022 wildfire and an image in the summer of 2023 were acquired for comparison consistency to observe the vegetation recovery in the same season (Table 1). All 12-unit bands in Sentinel-2A imagery were selected, while B1 and B9 were excluded as they are relevant for atmospheric study instead of land surface study, and there is no B10 in Level-2A imagery.

Table 1. Sentinel-2A imagery applied in this study.

Acquisition Date	Event	Cloud Cover (%)
2 August 2022	Pre-wildfire 2022	0.000657
26 September 2022	Post-wildfire 2022	0.152309
28 July 2023	Summer 2023 (1 Year after fire)	0.000352

Spectral indices were performed with *ee.Image.normalizedDifference()* in GEE for both NBR and NDVI. NBR was computed to detect the burnt area before and after the 2022 wildfire. The dNBR was applied to observe the fire severity of the 2022 wildfire. The polygon of the major burnt area derived from dNBR before and after the 2022 wildfire was exported to be used as the scope of the study area for further analysis. The fire severity of the major burnt area in the ROI was classified according to the dNBR value range proposed by Mediterranean local conditions (MLC) [61] and the United States Geological Survey (USGS) [62].

NDVI is one of the most used vegetation indices to quantify green vegetation and monitor vegetation health in agriculture, forestry, and ecology [63]. This study used NDVI to observe the vegetation dynamics between pre-wildfire 2022, post-wildfire 2022, and summer 2023. The results provide valuable information for vegetation loss after the 2022

wildfire and vegetation recovery in the summer of 2023. Subsequently, the NDVI was classified according to the NDVI value range proposed by USGS [64].

The Land Use and Occupation Map (COS) was published between 3 and 5 years from 1995 to 2018 in Portugal by *Direção Geral do Território* (DGT). The COSc has been published annually since 2018 as complementary information to COS. Both COS and COSc are products of the Land Occupation Monitoring System (SMOS), an innovative initiative designed and developed by the General Directorate of Territory (DGT) [29,30]. The COS serves as the primary reference cartography for planning, while the COSc demonstrates the land occupation that is not the land use in a specific year. COS is prepared in vector format at a scale of 1:25,000 with 44 classes of LULC, with an exception where COS2018 v2.0 has 83 classes of LULC [30]. On the other hand, COSc is available in raster format with 10 m pixels with 6, 9, and 13 classes at levels 1, 2, and 3, respectively. In contrast, subsequent maps have 15 classes at level 3, with improvement in the agriculture class [29]. COSc 2023 was classified based on a spectral database of monthly means in addition to spectral indices and intra-annual metrics from October 2022 to September 2023. The training database was processed with auxiliary information and photo interpretation and further classified with space technologies and artificial intelligence. COSc was used as the reference map for the land cover classification in this study to ensure consistency in validating the summer 2023 maps with COSc 2023.

The study area covers 15 classes at level 3 and 6 classes at level 1, referring to COSc. Referring to COSc 2021 and 2022, shrub and spontaneous herbaceous vegetation were prominent land covers in the study area. It was difficult to distinguish them at level 3 due to their remarkably similar spectral reflectance. Furthermore, it is challenging to classify the land cover classes as detailed as at level 3 solely based on red, green, and blue (RGB) composition and NDVI results. In addition, Ma et al. studied the fact that large classes reduce the accuracy of classification [65]. Hence, features with a high correlation were merged based on their COSc classes at level 1 for further analysis (Table 2).

Table 2. Description of the 6 land cover classes used in this research.







ID	Class/Level 1	Level 3	Satellite Image
0	2—Agriculture	211—Autumn/winter annual crops 212—Spring/summer annual crops 213—Other agricultural areas	
1	1—Artificial	100—Artificial areas	
2	5—Bareland	500—Surface without vegetation	

Table 2. Cont.

ID	Class/Level 1	Level 3	Satellite Image
3	3—Forest	311—Cork oak and holm oak 312—Eucalyptus 313—Other hardwoods 321—Maritime pine 323—Other resinous plants	
4	4—Shrub	410—Shrub 420—Spontaneous herbaceous vegetation	
5	6—Water	620—Water	

2.3. Methodology

This section outlines the step-by-step approach (Figure 2) applied to compare RF and SVM algorithms, with the processing primarily conducted on the GEE platform for land cover classification and burnt area recovery detection in the study area. The approach begins with data acquisition and pre-processing, followed by feature extraction using RGB composition and NDVI results. The feature collections are then processed with PBIA and OBIA for land cover classification. Subsequently, the samples are further split to train/test sets to train the classifiers for land cover classification in the ROI. The accuracy of the final land cover classification is assessed with evaluation metrics and validation techniques. The land cover maps with the highest accuracy are exported to QGIS 3.28 software for further spatial analysis, burnt area recovery detection, and map visualization.

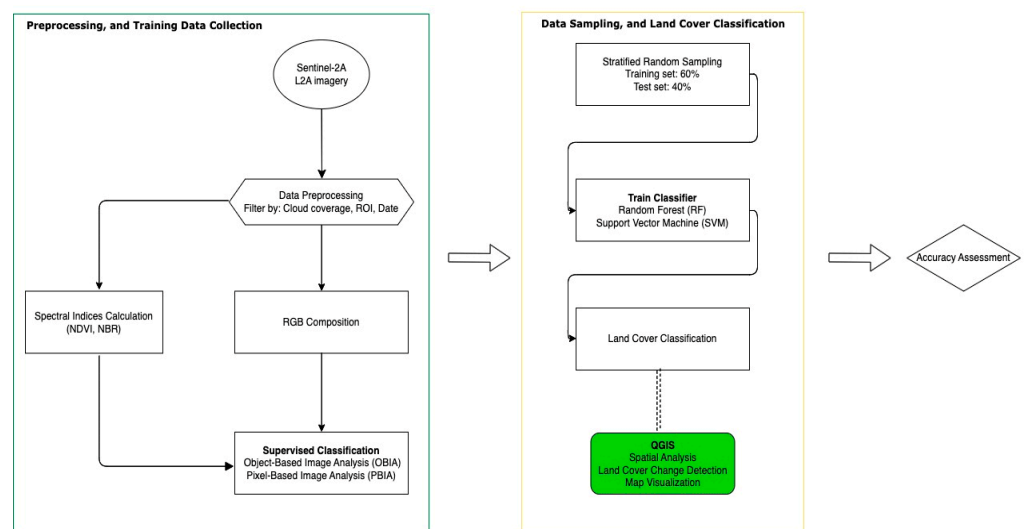


Figure 2. Methodology diagram.

2.3.1. Dataset Creation

PBIA and OBIA are widely used for land cover classification in RS applications [51–54,66]. This study used RGB composition and NDVI results to collect the features manually. The features were drawn in polygon because point-based samples tend to be more unstable [65]. Subsequently, the features were grouped into 6 feature collections, as categorized in Table 2 (Section 2.2). As sample size does not guarantee dataset accuracy [65], 100 features were collected for all land cover classes except for the water class, which occupied an insignificant area within the ROI. The 6 feature collections were combined into a single feature collection using the *ee.FeatureCollection()* function to unify all samples of all the land cover classes for data training and validation purposes. Images were sampled at a 20 m resolution for both PBIA and OBIA approaches using *ee.Image.sampleRegions()*. The scale parameter was set at a 20 m resolution after some experiments. A lower scale was computationally expensive and tended to be overfitting the samples.

PBIA classification was performed with different classifiers for land cover classification in urban [53] and forest areas [52]. These models produced land cover classification with satisfactory accuracy, which justified the inclusion of the PBIA approach in developing the best model to classify the land cover in the study area.

The Simple Non-Iterative Clustering (SNIC) algorithm on GEE was used for OBIA segmentation. SNIC is a bottom-up, seed-based segmentation algorithm that groups neighboring pixels based on spatial data and proximity similarity into clusters. The seeds are the initial points where the clusters grow and are spaced evenly across the image based on the parameter set [67]. There were large homogeneous areas, such as forest and bare land, and fine details, such as artificial areas, shrublands, and water, so a balance between the grid spacing was crucial. After some experiments, the parameter of 20 pixels was set for the spacing between seeds to be able to capture the feature details while not over-segmenting the image. The grid's shape was hexagonal to minimize the distances and increase the uniform distribution between neighboring seeds. The compactness was set to 0 to enable accurate segmentation based on the intrinsic characteristics (spectral and textural features) instead of the spatial proximity due to the diversified classes and irregular shape of land cover in the study area [59].

2.3.2. Classification

The samples generated were split into training and test datasets in a 60:40 ratio using *ee.ImageCollection.randomColumn()*. This provided datasets to train RF and SVM algorithms for land cover classification through stratified random sampling. After testing datasets with different decision tree sizes, the parameter was set to 30 for the RF classifier to optimize the land cover classification using *ee.Classifier.smileRandomForest()*. For the SVM classifier, the default setting of *ee.Classifier.libsvm()* on GEE was employed. The default Radial Basis Function (RBF) kernel was effective for various classification tasks, including land cover classification [37,68,69]. Also, Yousefi et al. found that variation in the gamma values did not affect the land cover classification accuracy [36]. Subsequently, the trained classifiers were applied to classify the land cover of the 3 images. Hence, 4 models were applied to each imagery type, which produced 12 land cover maps in total: (a) RF × OBIA, (b) RF × PBIA, (c) SVM × OBIA, and (d) SVM × PBIA. All the land cover maps were reprojected to EPSG:3763.

2.4. Accuracy Assessment

The land cover maps produced by different models and the integration of LULC classifications (PBIA or OBIA) and classifiers (RF or SVM) were assessed and compared to identify the best model for land cover classification. Evaluation metrics included (a) confusion matrix, (b) F1 score, (c) OA, and (d) kappa coefficient, which were conveniently obtained using the *ee.ConfusionMatrix* function. Due to a lack of ground truth data, the resulting land cover maps were compared with NDVI maps for the pre-wildfire 2022 results,

burnt area 2022 from ICNF and dNBR maps for the post-wildfire 2022 results, and COSc 2023 from SNIG for summer 2023 results.

A confusion matrix is a table that summarizes the performance of a classification algorithm [70]. A confusion matrix was obtained using the *ee.ConfusionMatrix()* function. True positive (TP) is the assignment where the model correctly predicts the land cover classes. In contrast, true negative (TN) is the assignment where the model is wrongly assigned the land cover classes. On the other hand, commission error (false positive/FP) is a sample wrongly assigned to other land cover classes that it does not belong to, while omission error (false negative/FN) is a sample left out in the land cover class that it is supposed to be assigned. The values generated in the confusion matrix were further evaluated for precision and recall values, performed with *consumersAccuracy()* and *producersAccuracy()* on GEE, respectively.

While precision and recall values of different land cover classes might be inconsistent in accuracy ranking, the F1 score was measured to obtain an insight into the accuracy of each model in classifying the land cover classes. F1 score balances precision and recall by minimizing FP and FN [71]. F1 score has a value from 0 to 1, where 1 indicates perfect precision and recall while 0 means otherwise.

OA provides an overview of the overall accuracy of TP and TN relative to the total assignments [72]. OA has a value ranging between 0 and 1, where 1 represents the highest accuracy while 0 indicates no accuracy.

Kappa coefficient indicates the inter-rater reliability between the land cover classification [68]. The degree of agreement ranges between -1 and 1 , where 1 represents perfect agreement, 0 represents no agreement, and -1 represents an agreement worse than random.

2.5. Comparison of Classified Maps with Official Maps

The burnt territories—burnt area 2022 (BA22), prepared by the ICNF—were retrieved for land cover classification validation purposes. The extent of the major burnt area, derived from the dNBR before and after the 2022 wildfire, was compared with BA22 to validate the burnt area extent after the wildfire event. As BA22 lacks robustness in assessing land cover maps, the dNBR map was used to analyze the rationality of post-wildfire land cover change relative to fire severity.

The NDVI map generated for the pre-wildfire event was compared with the land cover maps classified by different models for the same event to assess if the land size of the land cover reflected the vegetation conditions of the study area and examine the spatial data's consistency.

COSc 2023 was obtained from SNIG to compare with land cover maps of summer 2023. The land cover classes in COSc 2023 were visualized at COSc level 1, as illustrated in Table 1, to make the maps comparable.

The land cover maps generated by the models were exported to QGIS software for further analysis. The land cover maps were first clipped with the major burnt area extent. Descriptive statistics of NDVI and NBR, land area size according to spectral indices, and land cover classes of the study area were computed. Land cover maps of the study area's pre-wildfire 2022, post-wildfire 2022, and summer 2023 were intersected to detect the land cover change.

3. Results

3.1. Spectral Indices

The study area primarily experienced moderate and high degrees of fire severity in the 2022 wildfire, according to the dNBR classification proposed by both MLC and USGS (Figure 3). Furthermore, the difference between low and moderate fire severity areas classified by MLC and USGS was significant, resulting from the threshold differences. According to USGS's classification, 49.23% and 12.05% of the study area experienced moderate and low degrees of fire severity. In comparison, 43.03% and 16.89% of the study area experienced moderate and low degrees of fire severity according to MLC's

classification (Table 3). In both classifications, unburnt areas and areas affected by high fire severity occupied around 2% and 37%, respectively (Table 3).

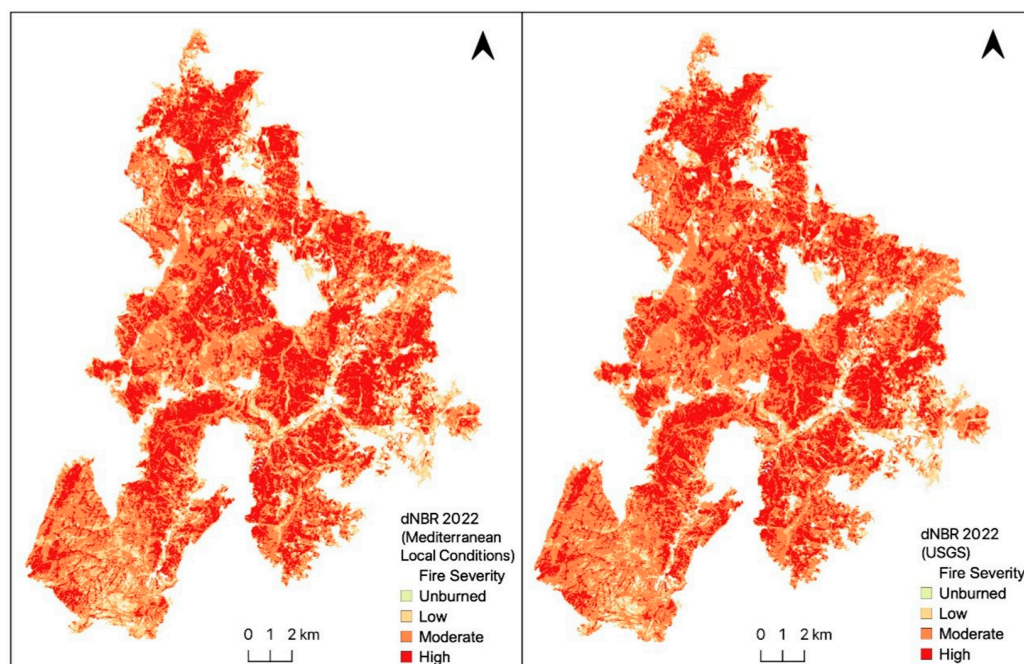


Figure 3. The dNBR maps of the study area for the 2022 wildfire, based on classifications proposed by MLC (left), and USGS (right).

Table 3. Analysis of the land area affected by different fire severities in the study area after the 2022 wildfire, based on the dNBR ranges proposed by MLC and USGS.

Fire Severity	dNBR Range (Scaled by 10 ³)	MLC (100 m ²)	%	dNBR Range (Scaled by 10 ³)	USGS (100 m ²)	%
Unburn	≤100	53,291	2.20	≤100	53,291	2.20
Low	100–320	409,450	16.89	100–270	292,044	12.05
Moderate	320–650	1,042,929	43.03	270–660	1,193,272	49.23
High	>650	918,192	37.88	>660	885,255	36.52
Total		2,423,862	100		2,423,862	100

Figure 4 presents the NDVI maps of the study area computed from Sentinel-2A data and classified according to USGS.

As shown in Figure 4a, the study area was predominantly occupied by dense vegetation before the wildfire event. About 98% of the study area experienced low to high fire severity during the 2022 wildfire (Table 4). The study area was occupied with sparse vegetation and had little dense vegetation after the wildfire. On the NDVI map of summer 2023 (Figure 4c), vegetation recovery was observed, especially in the top north. The land area of dense vegetation validated the vegetation dynamic of the study area along the events where dense vegetation occupied 65.12% of the study before the wildfire, reduced to 7.04% after the wildfire, and recovered to 23.84% in summer 2023 (Table 4). Meanwhile, the sparse vegetation increased from 34.85% to 91.98% after the 2022 wildfire and reduced to 75.11% in the summer of 2023 (Table 4). The area with no vegetation within the study area remained around 1% and less in all events (Table 4).

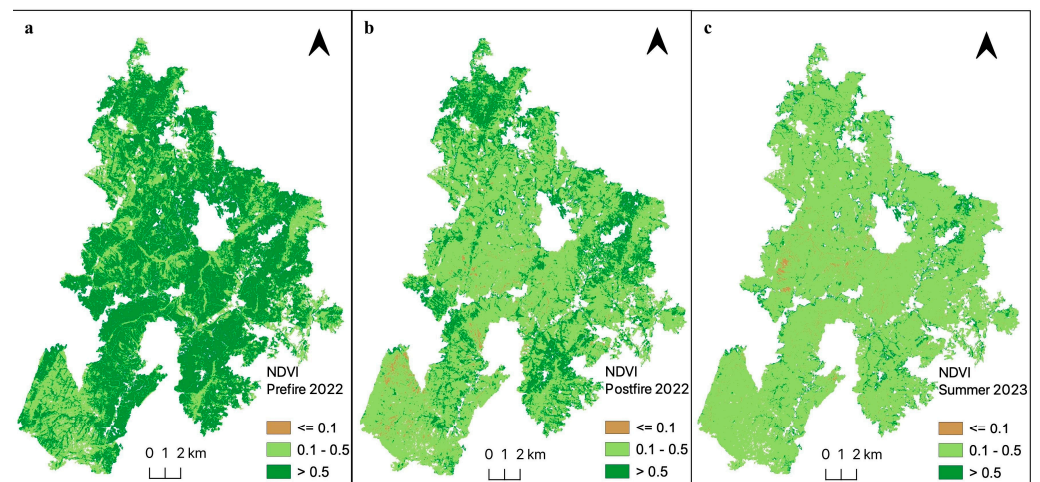


Figure 4. NDVI maps of the study area for (a) pre-wildfire 2022, (b) post-wildfire 2022, and (c) summer 2023. Computation was performed from Sentinel-2A data and classified according to the NDVI value range suggested by USGS.

Table 4. Analysis of the study area size subject to NDVI values range suggested by USGS.

NDVI	Pre-Wildfire 2022 (100 m ²)	%	Post-Wildfire 2022 (100 m ²)	%	Summer 2023 (100 m ²)	%
≤0.1	647	0.03	23,563	0.98	25,378	1.05
0.1–0.5	844,708	34.85	2,229,573	91.98	1,820,739	75.11
>0.5	1,578,507	65.12	170,726	7.04	577,745	23.84
Total	2,423,862	100	2,423,862	100	2,423,862	100

3.2. Evaluation Metrics for Random Forest and SVM

The confusion matrix tables show that the RF × OBIA model achieved the highest accuracy in land cover classification for the study area in all events (Tables S1–S3). This model distinguishes different land cover classes in all events except for Shrub. The Shrub was always misclassified with Agriculture interchangeably, particularly with models using the PBI approach. The misclassification in the post-wildfire result generated by the SVM × PBI model was weighty, where 223 samples (69.91%) were misclassified as Agriculture (Table 5). This far exceeds the 83 samples that were classified correctly for Shrub. Consequently, the classification of Shrub and Agriculture achieved a precision value of 0.2602 and a recall value of 0.6459 in this event. However, the precision and recall values for the Shrub classified by the RF × OBIA model were satisfactory. Furthermore, misclassification between Agriculture and Forest was generally noticeable in the PBI approach. However, land cover classification of pre-wildfire generated by the SVM × OBIA model demonstrated 770 samples misclassified as Forest instead of Agriculture, resulting in a low precision value of 0.6266 and recall value of 0.4787 for Forest and Agriculture, respectively.

Table 5. Confusion matrix of SVM × PBI model [Post-wildfire 2022].

SVM × PBI	Agriculture	Artificial	Bareland	Forest	Shrub	Water	Precision
Agriculture	797	2	16	249	79	0	0.6973
Artificial	11	207	6	0	0	0	0.9241
Bareland	18	13	2554	0	0	0	0.988
Forest	185	0	0	860	11	0	0.8144
Shrub	223	2	0	11	83	0	0.2602
Water	0	0	0	0	0	53	1
Recall	0.6459	0.9241	0.9915	0.7679	0.4798	1	

The F1 score was also used to evaluate the balances of the precision and recall values of the land cover classification generated by each model. Water achieved an F1 score of 1, indicating perfect precision and recall values in all models (Figure 5). This was expected as the spectral reflectance of Water is significantly different from other land covers. Regardless of the models, Bareland and Forest were classified precisely, especially in the RF × OBIA model (Tables S4–S6), where the F1 score was close to 1 in all events. The classification of Shrub achieved the lowest F1 score with the SVM × PBIA model in all events. While none of the F1 scores were higher than 0.634 with the SVM × PBIA model, the classification for Shrub, after the 2022 wildfire, achieved the lowest values of 0.3374, 0.2602, and 0.4798 for F1 score, precision, and recall, respectively (Tables S7–S9). Furthermore, Agriculture obtained the lowest F1 score with the SVM classifier in pre-wildfire events (Table S7) and as low as 0.6015 and 0.6151 for the OBIA and PBIA approaches, respectively. It is challenging to classify vegetation as the different types have very similar spectral reflectance [47]. Figure 5 presents the F1 score of the land covers according to their ranking in each model. Interestingly, OBIA and PBIA performed consistently with both RF and SVM classifiers in F1 score ranking for classification in post-wildfire 2022 and summer 2023. Hence, choosing the right classifier is vital to increasing land cover classification accuracy. Overall, RF had a relatively stable performance compared to SVM, as land cover classification accuracy using SVM fluctuated significantly among different scenarios. This was observed from the samples classified for Artificial, where high accuracy was achieved in the pre-wildfire event, while lower accuracy was attained in other events (Figure 5).

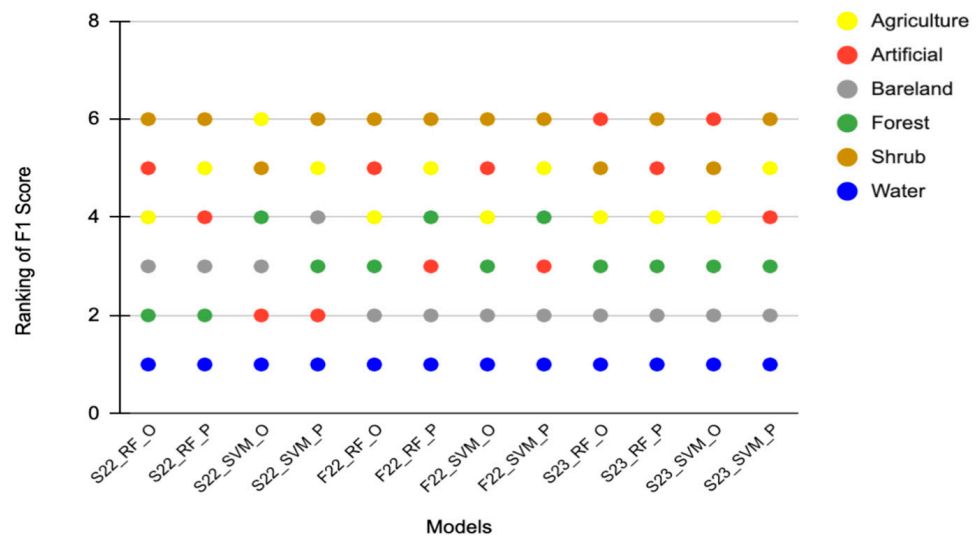


Figure 5. F1 score ranking for different land cover classes across various models.

Table 6 presents the OA and kappa coefficient of each model. The OA and kappa coefficient values aligned with the results found in the confusion matrix. The RF × OBIA model achieved the highest accuracy where the OA value was 0.99, and the kappa coefficient value was higher than 0.98 in all events. The RF classifier achieved higher OA and kappa coefficient values than the SVM classifier in most events, except for summer 2023. The SVM × OBIA model attained exceptional accuracy with an OA of 0.97 and a kappa coefficient of 0.96 for the land cover classification of summer 2023, outperforming the RF × PBIA model. Table 6 shows that the performance of the SVM classifier with both LULC approaches was not stable; one was better than the others in different events.

Table 6. Overall accuracy and kappa coefficient of each model.

	RF × OBIA		RF × PBIA		SVM × OBIA		SVM × PBIA	
	OA	κ	OA	κ	OA	κ	OA	κ
Pre-fire 2022	0.99	0.98	0.90	0.86	0.74	0.66	0.81	0.73
Post-fire 2022	0.99	0.98	0.94	0.91	0.84	0.76	0.85	0.77
Summer 2023	0.99	0.99	0.94	0.91	0.97	0.96	0.88	0.83

3.3. Comparison of Land Cover Classification Accuracy

Land cover maps of post-wildfire 2022, classified by different models, are presented in Figure 6. The burnt territories (BA22) shapefile retrieved from ICNF is highlighted in red borders. The land cover map classified by the RF × OBIA model (Figure 6a) reflects the fire severity better. Furthermore, 20,512.27 ha (Table 7) of Bareland classified by the RF × OBIA model is closest to the total area that experienced moderate and high degrees of fire severity, 19,611.21 ha (MLC) and 20,785.27 ha (USGS) as indicated in Table 3. Nevertheless, the smaller Bareland size classified by the SVM × PBIA model was due to the larger agricultural land in the study area, which was proven to be more fire-resistant. Thus, BA22 and dNBR were inadequate for comparing the accuracy of post-wildfire land cover maps.

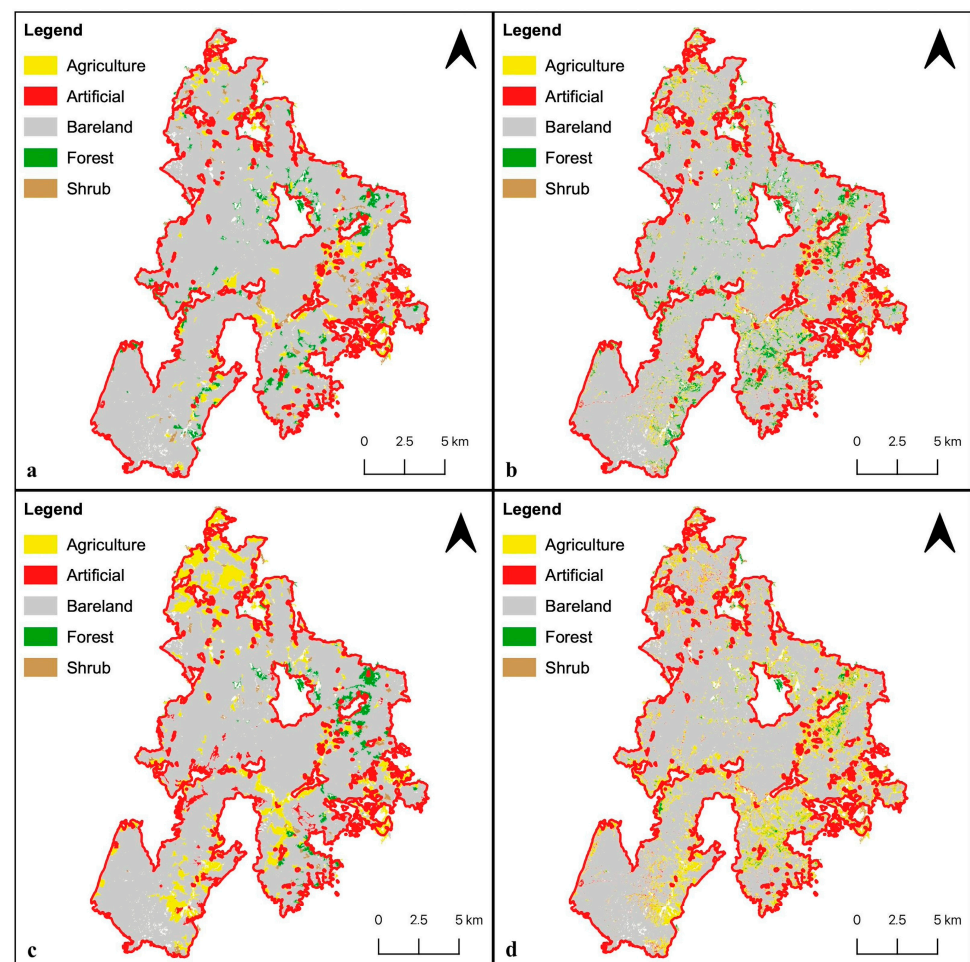


Figure 6. Comparison of the burnt area retrieved from ICNF (red border), and the post-wildfire land cover maps classified by different models: (a) RF × OBIA, (b) RF × PBIA, (c) SVM × OBIA, (d) SVM × PBIA.

Table 7. Analysis of the land cover size after wildfire 2022 for each model.

F22	RF × OBIA		RF × PBIA		SVM × OBIA		SVM × PBIA	
Class	Area (ha)	%	Area (ha)	%	Area (ha)	%	Area (ha)	%
0	1655.68	6.83	2989.13	12.33	3684.57	15.20	5172.30	21.34
1	191.49	0.79	373.98	1.54	639.68	2.64	593.50	2.45
2	20,512.27	84.63	18,566.33	76.60	18,710.02	77.19	17,346.21	71.56
3	1152.91	4.76	1527.02	6.30	754.61	3.11	391,02	1.61
4	724.23	2.99	779.75	3.22	447.71	1.85	733.09	3.02

Figure 7 presents the land cover maps of pre-wildfire 2022, classified by the different models proposed. They were compared with the NDVI map of pre-wildfire 2022 (Figure 4a). Land cover maps classified by RF × PBIA (Figure 7b) and SVM × PBIA (Figure 7d) were observed to be more consistent with the NDVI map. The study area had no vegetation (0.03%), sparse vegetation (34.85%), and dense vegetation (65.12%) before the 2022 wildfire (Table 4). The PBIA maps (Figure 7b,d) presented a smaller area for Agriculture, Artificial, and Bareland, and a larger area for Forest and Shrub than the OBIA maps (Figure 7a,c). The land cover map classified by the RF × OBIA model (Figure 7a,c) indicated an unusual Bareland area compared to the NDVI map (Figure 4a) in the southwestern of the study area. Given the comparison with the NDVI map and the land cover size analysis, the land cover map classified by the SVM × PBIA model reflected the pre-wildfire land cover more precisely.

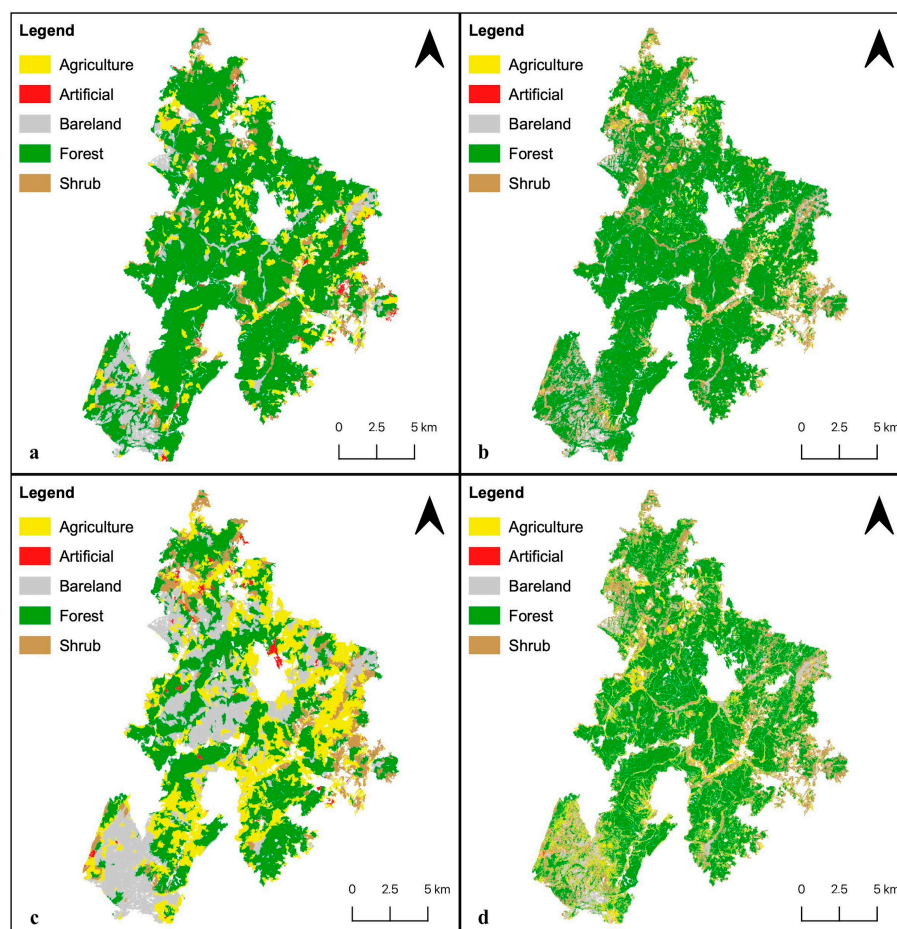


Figure 7. Comparison of land cover maps classified by different models: (a) RF × OBIA, (b) RF × PBIA, (c) SVM × OBIA, (d) SVM × PBIA for pre-wildfire 2022.

Figure 8 presents COSc 2023, where the study area was majorly recovered to Shrub with minor Agriculture and Forest regeneration while a smaller area of Bareland remained. Compared to the maps of Figure 9, land cover maps classified by the PBIA approach (Figure 9b,d) reflect the burnt area recovery and regeneration of forest more precisely. This is further confirmed by the land cover analysis presented in Table 8, in which the land size of Bareland and Forest classified by the PBIA approach is closer to the COSc 2023 classification than the land cover maps classified by the OBIA approach. Table 8 details that all models classified a much larger area of Agriculture and Artificial land and a much smaller Shrub compared to COSc 2023. Pertaining to the comparison of COSs 2023 with land cover maps of summer 2023, the SVM \times PBIA map (Figure 9d) closely resembles COSc 2023 (Figure 8), except that the major Shrub area in COSc 2023 is classified as Agriculture on the map.

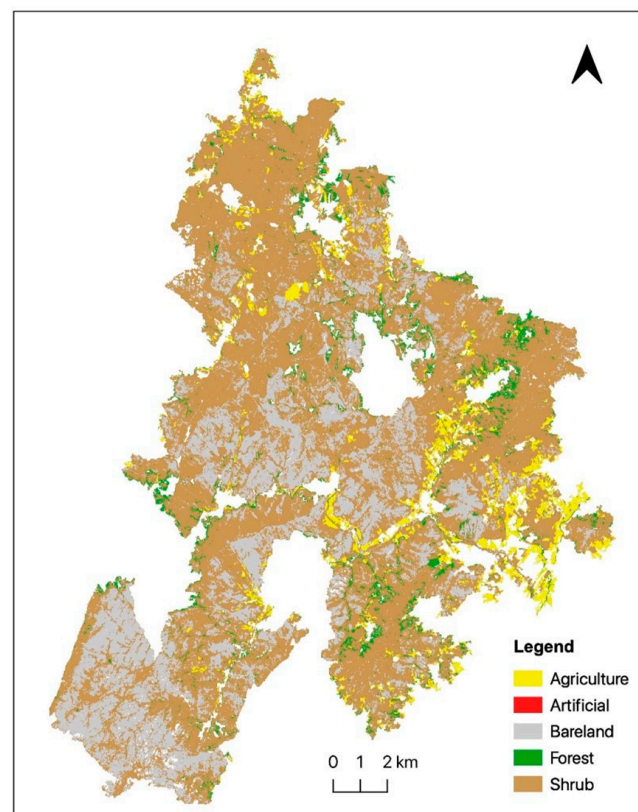


Figure 8. COSc 2023.

Table 8. Analysis of the land cover size in summer 2023 for each model and COSc 2023.

Area (ha)	Agriculture	Artificial	Bareland	Forest	Shrub
COSc 2023	1479.32	5.78	5820.55	1168.25	15,757.47
RF_OBIA_S23	6867.58	349.50	10,425.99	2316.96	4276.57
RF_PBIA_S23	10,254.29	187.83	8555.31	1892.89	3342.48
SVM_OBIA_S23	9822.13	1041.57	9404.46	2196.01	1771.86
SVM_PBIA_S23	14,189.20	472.56	7944.88	752.46	876.15

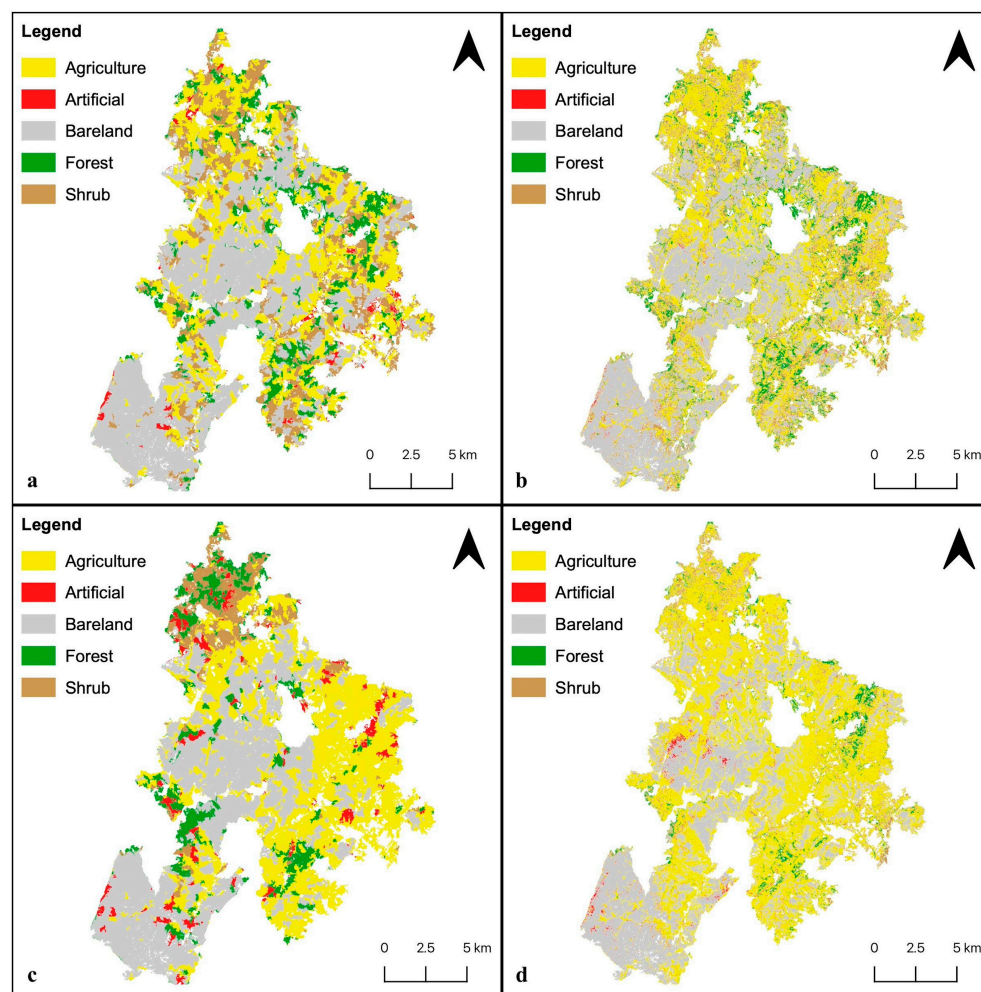


Figure 9. Comparison of land cover maps classified by different models: (a) RF \times OBIA, (b) RF \times PBIA, (c) SVM \times OBIA, (d) SVM \times PBIA for summer 2023.

3.4. Post-Wildfire Land Cover Change Detection

Following the results in Sections 3.2 and 3.3, where the RF \times OBIA model indicated the highest accuracy in all events among the models while the SVM \times PBIA model reflected better visual accuracy against the NDVI map and COSc 2023, land cover change detection was observed for both models. All the land cover classes had major changes to Bareland, which was ecologically reasonable after 98% (Table 3) of the study area was burnt in the wildfire event. According to the land cover change detected by the RF \times OBIA model (Table 9), 75.98% of the land cover changed to Bareland post-wildfire, where the paramount area was originally Forest that formed 65.38% of the study area. Consequently, 84.63% of the study area was covered by Bareland after the 2022 wildfire (Table 9). A significant size of the study area remained Bareland (41.11%) in summer 2023 (Table 9). While most of the land cover remained, there was remarkable regeneration of Agriculture, Forest, and Shrub, particularly in the north and east of the study area (Table 9). As for land cover change detected by the SVM \times PBIA model (Table 10), 67.94% of the land cover changed to Bareland after the 2022 wildfire, making up 71.56% of Bareland in the study area, of which forest was originally 46.92% of the study area. Furthermore, greater burnt area recovery was noticed from the land cover change of summer 2023 in the SVM \times PBIA model. It demonstrates a major Agriculture regeneration and a minor Forest and Shrub regeneration. There was major Agriculture regeneration from each land cover class, particularly 38.59% of the study area was recovered from Bareland to Agriculture, except for Forest (Table 10).

Table 9. Each land cover class’s major land cover change from pre-fire 2022 to post-fire 2022, and from post-fire 2022 to summer 2023 [RF × OBIA model].

Major Change from	Pre-Fire 2022 to Post-Fire 2022			Post-Fire 2022 to Summer 2023		
	to	Area (ha)	%	to	Area (ha)	%
Agriculture	Bareland	1593.07	6.57	Agriculture	690.74	2.85
Artificial	Bareland	70.53	0.29	Artificial	58.79	0.24
Bareland	Bareland	2094.21	8.64	Bareland	9965.35	41.11
Forest	Bareland	15,847.11	65.38	Forest	653.9	2.7
Shrub	Bareland	907.34	3.74	Agriculture	302.43	1.25

Table 10. The major land cover change of each land cover class from pre-fire 2022 to post-fire 2022 and from post-fire 2022 to summer 2023 [SVM × PBIA model].

Major Change from	Pre-Fire 2022 to Post-Fire 2022			Post-Fire 2022 to Summer 2023		
	to	Area (ha)	%	to	Area (ha)	%
Agriculture	Bareland	3305.88	13.64	Agriculture	3881.37	16.01
Artificial	Bareland	28.07	0.12	Agriculture	370.35	1.53
Bareland	Bareland	877.69	3.62	Agriculture	9354.4	38.59
Forest	Bareland	11,373.65	46.92	Forest	243.37	1
Shrub	Bareland	1760.7	7.26	Agriculture	450.55	1.9

3.5. Land Cover Maps

3.5.1. Land Cover Maps—RF × OBIA Model

Figure 10 presents the land cover maps classified by the RF × OBIA model for the three events. The land cover change is visually noticeable throughout the events. As shown in Figure 10a and Table 11, the study area was predominantly covered by forest (73.64%) with a considerable size of Bareland (9.31%) in the southwest area, while Agriculture (10.12%) and Shrub (6.22%) spread across the study area before the wildfire. As a consequence of the 2022 wildfire, the study area attained 84.63% of Bareland, resulting in minor vegetation of Agriculture (6.83%), Forest (4.76%), and Shrub (2.99%) as presented in Figure 10b and Table 11. Nearly half of the Bareland in the post-wildfire event was recovered in the summer of 2023 (Figure 10c). Regeneration of vegetation was reflected in the land cover change (Table 11): Agriculture (28.34%), Shrub (17.65%), and Forest (9.56%). The recovery was noticeable across the study area in the summer of 2023 (Figure 10c). Moreover, Artificial remained the smallest (not more than 1.44%, Table 11) land cover within the study area. Furthermore, Forest and Shrub were observed to be vulnerable to wildfire, with 93.54% and 51.93% of their land cover burnt in the 2022 wildfires, respectively (Table 11). On the other hand, Agriculture was more fire-resistant, with 32.5% of its land cover burnt in the wildfire event (Table 11).

Table 11. Land cover changes: pre-fire 2022, post-fire 2022, and summer 2023 [RF × OBIA].

ID	Land Cover	Pre-Fire 2022		Post-Fire 2022		Summer 2023	
		Area (ha)	%	Area (ha)	%	Area (ha)	%
0	Agriculture	2452.94	10.12	1655.68	6.83	6867.58	28.34
1	Artificial	173.57	0.72	191.49	0.79	349.5	1.44
2	Bareland	2256.58	9.31	20,512.27	84.63	10,425.99	43.02
3	Forest	17,846.92	73.64	1152.91	4.76	2316.96	9.56
4	Shrub	1506.59	6.22	724.23	2.99	4276.57	17.65
	Total	24,236.6	100	24,236.6	100	24,236.6	100

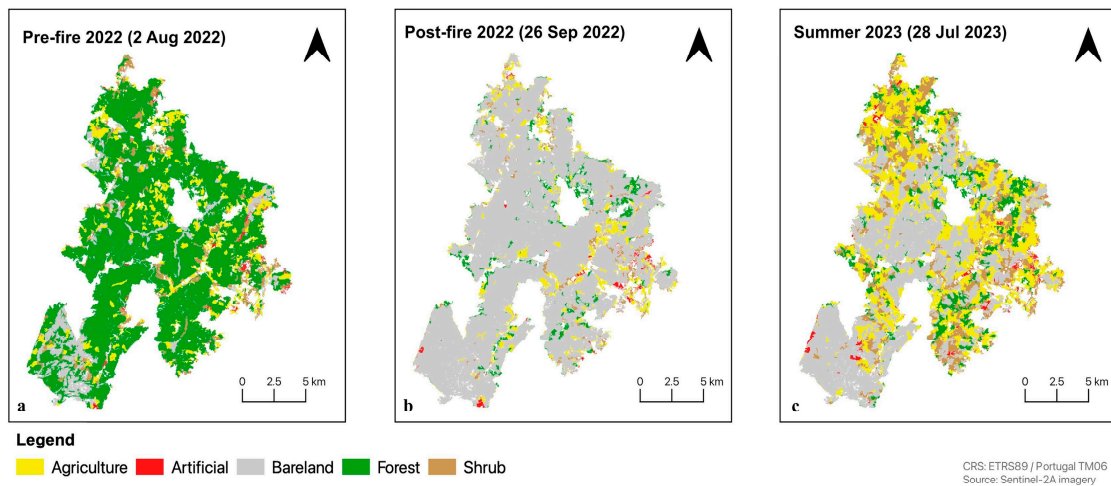


Figure 10. The land cover maps classified using the RF × OBIA model: (a) pre-wildfire 2022, (b) post-wildfire, and (c) summer 2023.

3.5.2. Land Cover Maps—SVM × PBI Model

Figure 11 presents the land cover maps classified by the SVM × PBI model for the three events. The land cover change is visually noticeable throughout the events. Figure 11a indicates that the study area was majorly covered with vegetation: Forest (61.41%), Agriculture (21.83%), and Shrub (12.42%), where Bareland (4.06%) and Artificial (0.26%) occupied less than 5% of the study area (Table 12) before the wildfire. As a consequence of the 2022 wildfire, the study area attained 71.56% of Bareland, which burned 97.37% and 75.65% of Forest and Shrub, respectively (Figure 11b and Table 12). This, again, proves the vulnerability of Forest and Shrub against wildfire. On the other hand, Agriculture was more fire-resistant, with 97.73% of its land cover preserved in the wildfire event (Table 12). More than half of the Bareland was recovered in the summer of 2023 (Figure 11c); major Agriculture regeneration was noticed where Agriculture occupied 58.55% of the study area while Forest (3.1%) had a smaller occupation than Shrub (3.62%) in the summer of 2023 (Table 12). Furthermore, the Artificial area remained the smallest (not more than 2.5%, Table 12) land cover within the study area.

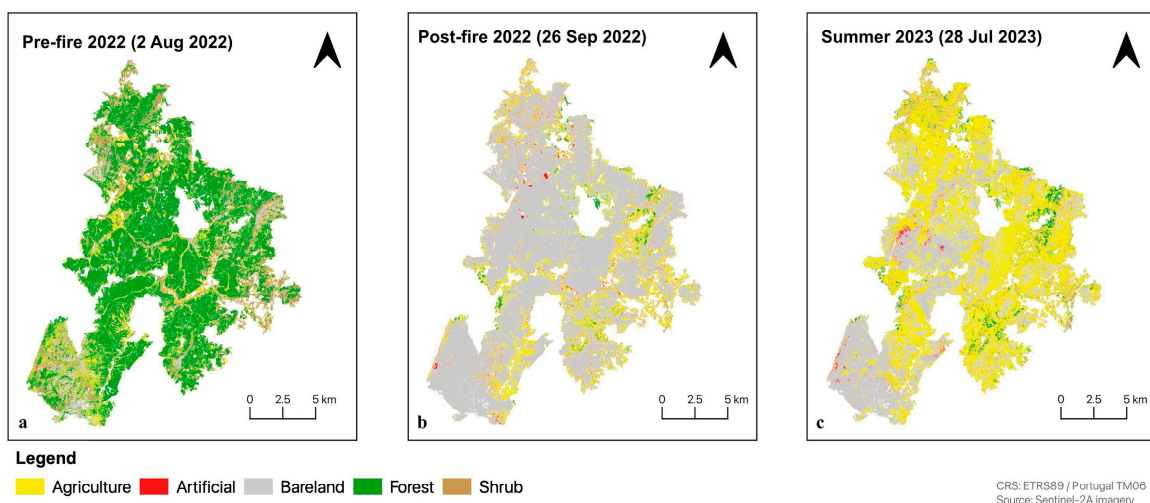


Figure 11. The land cover maps classified using the SVM × PBI model: (a) pre-wildfire 2022, (b) post-wildfire, and (c) summer 2023.

Table 12. Land cover changes: pre-fire 2022, post-fire 2022, and summer 2023 [SVM × PBIA].

ID	Land Cover	Pre-Fire 2022		Post-Fire 2022		Summer 2023	
		Area (ha)	%	Area (ha)	%	Area (ha)	%
0	Agriculture	5292.29	21.83	5172.30	21.34	14,189.20	58.55
1	Artificial	63.35	0.26	593.50	2.45	472.56	1.95
2	Bareland	984.99	4.06	17,346.21	71.56	7944.88	32.78
3	Forest	14,884.9	61.41	391.02	1.61	752.46	3.1
4	Shrub	3010.71	12.42	733.09	3.02	876.15	3.62
	Total	24,236.24	100	24,236.12	100	24,235.25	100

The RF × OBIA model (Figure 10a) indicated larger Forest and Bareland areas in pre-wildfire events. In contrast, the SVM × PBIA model (Figure 11a) indicated larger Agriculture and Shrub areas compared to each other. In addition, the RF × OBIA model (Figure 10b) demonstrated a larger Bareland. In comparison, the SVM × PBIA model (Figure 11b) showed slightly smaller Bareland with higher preservation of Agriculture land in the post-wildfire events. Both models confirm the vulnerability of Forest and Shrub against wildfire and prove the fire resistance of Agriculture. Furthermore, the SVM × PBIA model (Figure 11c) detailed a larger burnt area recovery with major Agriculture regeneration, while the RF × OBIA model (Figure 10c) demonstrated a smaller burnt area recovery with the regeneration of Agriculture, Shrub, and Forest in summer 2023.

4. Discussion

In this research, two LULC classification approaches, OBIA and PBIA, were integrated with RF and SVM classifiers, using GEE to optimize the land cover classification for the study area. Kappa coefficient was interpreted as an improvement upon OA [68]. RF classifier achieved almost perfect agreement of kappa results with both the OBIA and PBIA approaches. Unlike the RF classifier, the SVM classifier had relatively unstable performance, and the kappa results ranged from substantial to almost perfect agreement [68]. Referring to Figure 5, the OBIA and PBIA approaches were individually presented with similar F1 score rankings for both RF and SVM classifiers in each event. Hence, choosing the right classifier is vital to increase land cover classification accuracy. Furthermore, Shrub, the land cover class with the lowest F1 score in most events, was always misclassified, with Agriculture having a lower F1 score as well. The OBIA and PBIA approaches had difficulties classifying Shrub in all events, particularly with the SVM × PBIA model. In the RF × OBIA model, the accuracy for Shrub classification was still relatively high, with the F1 score above 0.91 in all events. The slight misclassification between Artificial and Shrub might be due to the characteristics of SNIC, considering the neighboring spatial feature. At the same time, sparse vegetation around the artificial land was common in the study area. In this regard, the parameter setting for SNIC is crucial. A lower scale is computationally expensive for large areas and unnecessary for large-scale homogeneous landscapes in the study area. The balance in determining an optimal distance unit among the land cover classes is critical. In addition, Shrub and Agriculture were misclassified interchangeably in all models with the PBIA approach. Furthermore, the SVM classifier could not classify Agriculture precisely with both OBIA and PBIA approaches for the study area. It is challenging to classify the vegetations, as they have very similar spectral reflectance [37,38,47]. The challenge of classifying the vegetation accurately remains a major concern, as there are three classes of vegetation in this research, and the capacity to classify the vegetation at lower levels is an asset to observing the vegetation dynamics and the recovery of biodiversity in the study area. According to the metric results, the RF × OBIA model achieved the highest accuracy, while the SVM models had a lower accuracy for land cover classification in all events. Regardless of the high accuracy examined by the evaluation metrics, the difference between the land cover maps and COSc 2023 was not assessable due to the inequivalence of the dataset.

In contrast to the metric results, the comparison of the NDVI map, dNBR map, and COSc 2023 showed a completely different finding. The SVM \times PBIA model, which had a lower value of evaluation metrics, demonstrated a more analogous visual result among the land cover maps. The pre-wildfire map classified by the SVM \times PBIA model (Figure 7d) corresponded to the NDVI map (Figure 4a) of the same event. This is logical as the NDVI map was produced by a pixel comparison of the NIR band and red band; even the RF \times PBIA map (Figure 7b) had better visual results than the RF \times OBIA map (Figure 7a). As for the comparison between dNBR and post-wildfire land cover maps, the RF \times OBIA map had the largest bare land among all the pre-wildfire maps (Table 7), and the bare land size was between the burnt area classified by MLC and USGS for moderate to high fire severity (Table 3). Nevertheless, a smaller bare land size classified by the SVM \times PBIA model (Table 7) was due to the larger agricultural land in the study area, which was proven to be more fire-resistant. In the case where field data are available, Relativized Burn Ratio (RBR) can be applied to improve the reliability of the fire severity assessment for the dataset validation as RBR increases the accuracy of the burn ratio for diverse vegetation densities by normalizing pre-fire conditions [73,74]. While dNBR was inadequate to compare the accuracy of post-wildfire land maps, the robustness of the RF \times OBIA model in capturing the burnt area effectively underscores its potential for ecological planning and vegetation recovery observation. The result concurs with Çömert et al.'s [75], where the RF \times OBIA model achieved an OA of 0.99 in mapping the burnt area in forest areas in Adrasan and Kumluca regions in Antalya province, Turkey. In addition, it was also concerning that more than 43% and about 37% of the study area experienced moderate and high fire severity, respectively (Table 3). Fire severity changes soil moisture, and it takes longer for new seeds to grow; this leads to a longer recovery after wildfires [76,77]. Moreover, soil erosion and runoff triggered landslides and flash floods after the wildfire [22]. In contrast, the ecosystem of the study area is affected in the long term as resprouting species regrow more quickly than seeder species [78]. This leads to species and habitat alteration and impacts the area's biodiversity [79]. Pertaining to the comparison of COSs 2023 with land cover maps of summer 2023, the SVM \times PBIA map (Figure 9d) closely resembled COSc 2023 (Figure 8), except that the major Shrub area in COSc 2023 was classified as Agriculture on the map.

There are inherent limitations to validation in this study. The discrepancies observed in Table 8, where the automated methods produced results that were not comparable to COSc 2023, are due to the differences in the temporal scales of the dataset. The land cover map generated in this research was based on a specific date, while the land cover classification in COSc 2023 was based on the monthly mean of a year [29]. Moreover, there were no ground truth data to validate whether the Agriculture on the SVM \times PBIA map for summer 2023 (Figure 9d) was correctly presented and whether the Shrub on COSc 2023 (Figure 8) indicated the vegetation dynamic after the agricultural harvest. Furthermore, we also could not test whether it was the failure of the SVM \times PBIA model for summer 2023 in distinguishing Shrub and Agriculture that caused the difference in the land cover. In addition, Tables 9 and 10 present remarkable differences in the results of major land cover change from pre-fire 2022 to post-fire 2022 and from post-fire 2022 to summer 2023. This is due to the different characteristics of the land classification approaches and ML algorithms used in the RF \times OBIA and the SVM \times PBIA models. Several studies found that the RF \times OBIA model achieved a high accuracy for land classification in agricultural land and forest region [43,80,81]. On the other hand, SVM was very sensitive to hyperparameter tuning and achieved fluctuating results when integrated with OBIA in Nielsen et al.'s study [82]. In contrast, the SVM \times PBIA model efficiently mapped the land cover for a densely vegetated and cultivated area [83]. After all, the NDVI map, dNBR map, and COSc 2023 were not the most adequate source data to serve as a solid comparison to examine the accuracy of the land cover maps. While there is no comparable dataset to identify a more reliable result between the two models, the evaluation metrics selected suggested that the RF \times OBIA model achieved the highest accuracy in all events among the models.

The limitation of a comparable dataset for accuracy validation is not unusual. Nasiri et al. [80] studied model generalization by calibrating two distinct sets of samples and proved the RF \times OBIA model to be effective for tree-cutting detection in forest districts. Because no ground truth data or solid comparisons are available, both RF and SVM classifiers are not justified to be reliable for monitoring the burnt area recovery in the study area even though RF \times OBIA maps indicated a high value of evaluation metrics and SVM \times PBIA maps are visually accurate compared to the NDVI map and COSc 2023. The output produced by both models was significantly different; it is arguable which model is more accurate for reference.

5. Conclusions

This research aimed to identify the best model for land cover classification of the study area using GEE. A land cover map provides important information for emergency planning and disaster management during a wildfire, as well as burnt areas and vegetation monitoring after a wildfire. Sentinel-2A imagery was processed with two LULC classification approaches, OBIA and PBIA. The feature collections were subsequently trained with RF and SVM classifiers on GEE. The land cover maps were compared with the NDVI, BA22, dNBR, and COSc 2023 maps. The evaluation metric results were consistent; the RF \times OBIA model was the most accurate for land cover classification in the study area. Compared with the NDVI map and COSc 2023, the SVM \times PBIA map resembled the maps better. However, the validation of land cover maps against COSc 2023 was not ideal as the land cover map generated in this research was based on a specific date, while the land cover classification in COSc 2023 was based on the monthly mean of a year. In addition, there was no access to field data, which are necessary for validation. Considering these limitations, the best model for land cover classification of the study area was not conclusively determined. While the study's best model for land cover classification was not determined, the findings demonstrated the strengths and limitations of different models. Moreover, this study represents the first application of such a comparative analysis in this study area, offering a methodological framework that can be applied to other Mediterranean or forest regions prone to wildfires, especially when rapid assessments are needed for emergency evaluations. In addition, this research provides some important insights: i) the land cover classification with the highest values of evaluation metrics might not reflect the same level of accuracy in map presentation; ii) concurrent with Lawrence and Moran's studies, more classifiers should be tested to identify the most accurate model; iii) the PBIA approach had difficulties in distinguishing the vegetation; the OBIA approach tackled this problem better with the RF classifier but not with the SVM classifier; and iv) the SVM classifier had unstable performance where the accuracy in classifying the land cover classes fluctuated in different events.

In future work, the research could build on this foundation by testing the models with additional imagery in response to the available field data or model generalization to identify an optimized model to classify the land cover for emergency evaluation and periodic assessment in the study area. Since the SVM \times PBIA model strongly resembled COSc 2023 while achieving a low accuracy in evaluation metrics, different parameters can be tested and refined to optimize the result in future work. Furthermore, different ML and deep learning algorithms can be tested to improve the land cover classification result.

Supplementary Materials: The following supporting information can be downloaded at: <https://www.mdpi.com/article/10.3390/land13111878/s1>, Table S1: Confusion matrix of RF \times OBIA model [pre-wildfire 2022]; Table S2: Confusion matrix of RF \times OBIA model [post-wildfire 2022]; Table S3: Confusion matrix of RF \times OBIA model [summer 2023]; Table S4: RF metric results for OBIA and PBIA approaches [pre-wildfire 2022]; Table S5: RF metric results for OBIA and PBIA approaches [post-wildfire 2022]; Table S6: RF metric results for OBIA and PBIA approaches [summer 2023]; Table S7. SVM metric results for OBIA and PBIA approaches [pre-wildfire 2022]; Table S8: SVM metric results for OBIA and PBIA approaches [post-wildfire 2022]; Table S9: SVM metric results for OBIA and PBIA approaches [summer 2023].

Author Contributions: Y.-C.T. conceived and conducted the study, performed the experiments, analyzed data, and wrote the manuscript, A.C.T. supervised the study, provided guidance, and proofread the manuscript; and L.D. assisted in revising and structuring the manuscript. All authors have read and agreed to the published version of the manuscript.

Funding: This research received no external funding.

Data Availability Statement: The original contributions presented in the study are included in the article/Supplementary Materials, further inquiries can be directed toward the corresponding author.

Acknowledgments: This work was supported by national funding awarded by FCT—Foundation for Science and Technology, I.P., projects UIDB/04683/2020 (<https://doi.org/10.54499/UIDB/04683/2020>) and UIDP/04683/2020 (<https://doi.org/10.54499/UIDP/04683/2020>).

Conflicts of Interest: The authors declare no conflicts of interest.

References

1. Szpakowski, D.M.; Jensen, J.L.R. A Review of the Applications of Remote Sensing in Fire Ecology. *Remote Sens.* **2019**, *11*, 2638. [[CrossRef](#)]
2. Bashirzadeh, M.; Abedi, M.; Shefferson, R.P.; Farzam, M. Post-Fire Recovery of Plant Biodiversity Changes Depending on Time Intervals since Last Fire in Semiarid Shrublands. *Fire* **2023**, *6*, 103. [[CrossRef](#)]
3. Calsamiglia, A.; Lucas-Borja, M.E.; Fortesa, J.; García-Comendador, J.; Estrany, J. Changes in Soil Quality and Hydrological Connectivity Caused by the Abandonment of Terraces in a Mediterranean Burned Catchment. *Forests* **2017**, *8*, 333. [[CrossRef](#)]
4. Papathanasiou, C.; Makropoulos, C.; Mimikou, M. Hydrological modelling for flood forecasting: Calibrating the post-fire initial conditions. *J. Hydrol.* **2015**, *529*, 1838–1850. [[CrossRef](#)]
5. Stoof, C.R.; Ferreira, A.J.D.; Mol, W.; Van den Berg, J.; De Kort, A.; Drooger, S.; Slingerland, E.C.; Mansholt, A.U.; Ferreira, C.S.S.; Ritsema, C.J. Soil surface changes increase runoff and erosion risk after a low-moderate severity fire. *Geoderma* **2015**, *239*, 58–67. [[CrossRef](#)]
6. Fournier, T.; Fèvre, J.; Carcaillet, F.; Carcaillet, C. For a few years more: Reductions in plant diversity 70 years after the last fire in Mediterranean forests. *Plant Ecol.* **2020**, *221*, 559–576. [[CrossRef](#)]
7. Lloret, F.; Vilà, M. Diversity patterns of plant functional types in relation to fire regime and previous land use in Mediterranean woodlands. *J. Veg. Sci.* **2003**, *14*, 387–398. [[CrossRef](#)]
8. Viana-Soto, A.; Okujeni, A.; Pflugmacher, D.; García, M.; Aguado, I.; Hostert, P. Quantifying post-fire shifts in woody-vegetation cover composition in Mediterranean pine forests using Landsat time series and regression-based unmixing. *Remote Sens. Environ.* **2022**, *281*, 113239. [[CrossRef](#)]
9. Dolny, A.; Ozana, S.; Burda, M.; Harabis, F. Effects of Landscape Patterns and Their Changes to Species Richness, Species Composition, and the Conservation Value of Odonates (Insecta). *Insects* **2021**, *12*, 478. [[CrossRef](#)]
10. Hasan, S.S.; Zhen, L.; Miah, M.G.; Ahamed, T.; Samie, A. Impact of land use change on ecosystem services: A review. *Environ. Dev.* **2020**, *34*, 100527. [[CrossRef](#)]
11. Wiersma, Y.F.; Nudds, T.D.; Rivard, D.H. Models to distinguish effects of landscape patterns and human population pressures associated with species loss in Canadian national parks. *Landsc. Ecol.* **2004**, *19*, 773–786. [[CrossRef](#)]
12. Tahiru, A.A.; Doke, D.A.; Baatuwue, B.N. Effect of land use and land cover changes on water quality in the Nawuni Catchment of the White Volta Basin, Northern Region, Ghana. *Appl. Water Sci.* **2020**, *10*, 198. [[CrossRef](#)]
13. Wear, D.N.; Turner, M.G.; Naiman, R.J. Land cover along an urban-rural gradient: Implications for water quality. *Ecol. Appl.* **1998**, *8*, 619–630.
14. Wilson, C.; Weng, Q. Assessing Surface Water Quality and Its Relation with Urban Land Cover Changes in the Lake Calumet Area, Greater Chicago. *Environ. Manag.* **2010**, *45*, 1096–1111. [[CrossRef](#)]
15. Alkama, R.; Cescatti, A. Biophysical climate impacts of recent changes in global forest cover. *Science* **2016**, *351*, 600–604. [[CrossRef](#)]
16. Feddema, J.J.; Oleson, K.W.; Bonan, G.B.; Mearns, L.O.; Buja, L.E.; Meehl, G.A.; Washington, W.M. The importance of land-cover change in simulating future climates. *Science* **2005**, *310*, 1674–1678. [[CrossRef](#)]
17. Seto, K.C.; Fragkias, M.; Güneralp, B.; Reilly, M.K. A Meta-Analysis of Global Urban Land Expansion. *PLoS ONE* **2011**, *6*, e23777. [[CrossRef](#)]
18. Houghton, R.A.; House, J.I.; Pongratz, J.; van der Werf, G.R.; DeFries, R.S.; Hansen, M.C.; Le Quéré, C.; Ramankutty, N. Carbon emissions from land use and land-cover change. *Biogeosciences* **2012**, *9*, 5125–5142. [[CrossRef](#)]
19. Zhao, M.; Pitman, A.J. The impact of land cover change and increasing carbon dioxide on the extreme and frequency of maximum temperature and convective precipitation. *Geophys. Res. Lett.* **2002**, *29*, 2-1–2-4. [[CrossRef](#)]
20. Eurostat. Archive: Land Cover and Land Use Statistics at Regional Level. Available online: https://ec.europa.eu/eurostat/statistics-explained/index.php?title=Archive:Land_cover_and_land_use_statistics_at_regional_level (accessed on 25 October 2023).

21. United States Environmental Protection Agency. Land Cover–Environmental Effects. Available online: <https://www.epa.gov/report-environment/land-cover#:~:text=Land%20cover%20affects%20or%20influences,,%20climate,%20and%20carbon%20storage> (accessed on 25 October 2023).
22. European Commission. Available online: <http://data.europa.eu/89h/9433731c-2c95-4588-b5fe-979d04633c29> (accessed on 13 June 2024).
23. European Forest Fire Information System. Available online: <https://effis.jrc.ec.europa.eu/apps/effis.statistics/estimates/EU/2024/2006/2023> (accessed on 25 October 2023).
24. Turco, M.; Jerez, S.; Augusto, S.; Tarín-Carrasco, P.; Ratola, N.; Jiménez-Guerrero, P.; Trigo, R.M. Climate drivers of the 2017 devastating fires in Portugal. *Sci. Rep.* **2019**, *9*, 13886. [CrossRef]
25. Euronews. Available online: <https://www.euronews.com/2022/09/13/eleven-people-acquitted-of-negligence-over-deadly-2017-wildfires-in-portugal> (accessed on 16 October 2023).
26. Diário de Notícias. Available online: <https://www.dn.pt/sociedade/incendio-de-agosto-foi-o-maior-em-47-anos-na-serra-da-estrela-15552358.html/> (accessed on 2 October 2023).
27. Burned Territories–Burned Area 2022. Available online: <https://sig.icnf.pt/portal/home/item.html?id=983c4e6c4d5b4666b258a3ad5f3ea5af> (accessed on 2 October 2023).
28. NaturalPT. Available online: <https://natural.pt/protected-areas/parque-natural-serra-estrela?locale=pt> (accessed on 6 November 2023).
29. COSc. SNIG. Available online: <https://snig.dgterritorio.gov.pt/rndg/srv/search?keyword=COSc> (accessed on 15 November 2023).
30. COS. SNIG. Available online: <https://snig.dgterritorio.gov.pt/rndg/srv/search?keyword=COS> (accessed on 15 November 2023).
31. Shrestha, B.B. Approach for Analysis of Land-Cover Changes and Their Impact on Flooding Regime. *Quaternary* **2019**, *2*, 27. [CrossRef]
32. Githui, F.; Mutua, F.; Bauwens, W. Estimating the impacts of land-cover change on runoff using the soil and water assessment tool (SWAT): Case study of Nzoia catchment, Kenya. *Hydrol. Sci. J.* **2009**, *54*, 899–908. [CrossRef]
33. Wu, S.; Li, D.; Liu, L.; Zhang, W.; Liu, K.; Zhao, W.; Shen, J.; Hao, C.; Zhang, L. Global patterns and influencing factors of post-fire land cover change. *Glob. Planet. Chang.* **2023**, *223*, 104076. [CrossRef]
34. Huang, X.; Jensen, J.R. A machine-learning approach to automated knowledge-base building for remote sensing image analysis with GIS data. *Photogramm. Eng. Remote Sens.* **1997**, *63*, 1185–1193.
35. Chen, L.C.; Papandreou, G.; Kokkinos, I.; Murphy, K.; Yuille, A.L. DeepLab: Semantic Image Segmentation with Deep Convolutional Nets, Atrous Convolution, and Fully Connected CRFs. *IEEE Trans. Pattern Anal. Mach. Intell.* **2018**, *40*, 834–848. [CrossRef] [PubMed]
36. Yousefi, S.; Mirzaee, S.; Almohamad, H.; Al Dughairi, A.A.; Gomez, C.; Siamian, N.; Alrasheedi, M.; Abdo, H.G. Image Classification and Land Cover Mapping Using Sentinel-2 Imagery: Optimization of SVM Parameters. *Land* **2022**, *11*, 993. [CrossRef]
37. Jia, Y. Object-Based Land Cover Classification with Orthophoto and Lidar Data. Available online: <https://www.diva-portal.org/smash/get/diva2:788855/FULLTEXT02.pdf> (accessed on 9 February 2024).
38. De Oliveira IC, L.B. Remote Sensing for Land Use/Land Cover Mapping in Almada. Master’s Thesis, NOVA University Lisbon, Lisbon, Portugal, 2022.
39. Aziz, G.; Minallah, N.; Saeed, A.; Frnda, J.; Khan, W. Remote sensing based forest cover classification using machine learning. *Sci. Rep.* **2024**, *14*, 69. [CrossRef]
40. Rodriguez-Galiano, V.F.; Ghimire, B.; Rogan, J.; Chica-Olmo, M.; Rigol-Sanchez, J.P. An assessment of the effectiveness of a random forest classifier for land-cover classification. *ISPRS J. Photogramm. Remote Sens.* **2012**, *67*, 93–104. [CrossRef]
41. Brnabic, A.; Hess, L.M. Systematic literature review of machine learning methods used in the analysis of real-world data for patient-provider decision making. *BMC Med. Inform. Decis. Mak.* **2021**, *21*, 54. [CrossRef]
42. MIT Sloan School of Management. Available online: <https://mitsloan.mit.edu/ideas-made-to-matter/machine-learning-explained#:~:text=What%20is%20machine%20learning?,to%20how%20humans%20solve%20problems> (accessed on 9 February 2024).
43. Maxwell, A.E.; Warner, T.A.; Fang, F. Implementation of machine-learning classification in remote sensing: An applied review. *Int. J. Remote Sens.* **2018**, *39*, 2784–2817. [CrossRef]
44. Dostmohammadi, M.; Pedram, M.Z.; Hoseinzadeh, S.; Garcia, D.A. A GA-stacking ensemble approach for forecasting energy consumption in a smart household: A comparative study of ensemble methods. *J. Environ. Manag.* **2024**, *364*, 121264. [CrossRef] [PubMed]
45. Roy, M.-H.; Larocque, D. Robustness of random forests for regression. *J. Nonparametric Stat.* **2012**, *24*, 993–1006. [CrossRef]
46. Contreras, P.; Orellana-Alvear, J.; Muñoz, P.; Bendix, J.; Célleri, R. Influence of Random Forest Hyperparameterization on Short-Term Runoff Forecasting in an Andean Mountain Catchment. *Atmosphere* **2021**, *12*, 238. [CrossRef]
47. Zhao, Y. Chapter 4—Decision Trees and Random Forest. In *R and Data Mining*; Zhao, Y., Ed.; Academic Press: Cambridge, MA, USA, 2013; pp. 27–40.
48. Chau, A.L.; Li, X.; Yu, W. Support vector machine classification for large datasets using decision tree and Fisher linear discriminant. *Future Gener. Comput. Syst.* **2014**, *36*, 57–65. [CrossRef]

49. Urso, A.; Fiannaca, A.; La Rosa, M.; Ravi, V.; Rizzo, R. Data Mining: Classification and Prediction. In *Encyclopedia of Bioinformatics and Computational Biology*; Ranganathan, S., Gribskov, M., Nakai, K., Schönbach, C., Eds.; Academic Press: Oxford, UK, 2019; pp. 384–402.
50. Xia, Y. Chapter Eleven—Correlation and association analyses in microbiome study integrating multiomics in health and disease. In *Progress in Molecular Biology and Translational Science*; Sun, J., Ed.; Academic Press: Cambridge, MA, USA, 2020; Volume 171, pp. 309–491.
51. Hossain, M.D.; Chen, D. Segmentation for Object-Based Image Analysis (OBIA): A review of algorithms and challenges from remote sensing perspective. *ISPRS J. Photogramm. Remote Sens.* **2019**, *150*, 115–134. [[CrossRef](#)]
52. Tassi, A.; Gigante, D.; Modica, G.; Di Martino, L.; Vizzari, M. Pixel- vs. Object-Based Landsat 8 Data Classification in Google Earth Engine Using Random Forest: The Case Study of Maiella National Park. *Remote Sens.* **2021**, *13*, 2299. [[CrossRef](#)]
53. Goldblatt, R.; You, W.; Hanson, G.; Khandelwal, A.K. Detecting the Boundaries of Urban Areas in India: A Dataset for Pixel-Based Image Classification in Google Earth Engine. *Remote Sens.* **2016**, *8*, 634. [[CrossRef](#)]
54. Xiong, J.; Thenkabail, P.S.; Tilton, J.C.; Gumma, M.K.; Teluguntla, P.; Oliphant, A.; Congalton, R.G.; Yadav, K.; Gorelick, N. Nominal 30-m Cropland Extent Map of Continental Africa by Integrating Pixel-Based and Object-Based Algorithms Using Sentinel-2 and Landsat-8 Data on Google Earth Engine. *Remote Sens.* **2017**, *9*, 1065. [[CrossRef](#)]
55. VisitPortugal. Available online: <https://www.visitportugal.com/en/destinos/centro-de-portugal/73759> (accessed on 13 November 2023).
56. Life-Relict. Available online: <http://www.liferelict.ect.uevora.pt/index.php/areas-de-intervencao/?lang=en> (accessed on 13 November 2023).
57. European Environment Agency. Available online: <https://eunis.eea.europa.eu/sites/PTCON0014> (accessed on 3 November 2023).
58. Estrela Geopark Association. Available online: <https://www.geoparkestrela.pt/menu> (accessed on 3 November 2023).
59. Google Earth Engine. Available online: <https://developers.google.com/earth-engine/apidocs/ee-algorithms-image-segmentation-snic> (accessed on 3 June 2024).
60. Google Earth Engine. Available online: <https://earthengine.google.com/faq/> (accessed on 3 June 2024).
61. Teodoro, A.; Amaral, A. A Statistical and Spatial Analysis of Portuguese Forest Fires in Summer 2016 Considering Landsat 8 and Sentinel 2A Data. *Environments* **2019**, *6*, 36. [[CrossRef](#)]
62. UN-SPIDER. Available online: <https://www.un-spider.org/advisory-support/recommended-practices/recommended-practice-burn-severity/in-detail/normalized-burn-ratio> (accessed on 5 December 2023).
63. Pettorelli, N. *The Normalized Difference Vegetation Index*; Oxford University Press: Oxford, UK, 2013.
64. USGS. Available online: <https://www.usgs.gov/special-topics/remote-sensing-phenology/science/ndvi-foundation-remote-sensing-phenology> (accessed on 12 September 2024).
65. Ma, L.; Li, M.C.; Ma, X.X.; Cheng, L.; Du, P.J.; Liu, Y.X. A review of supervised object-based land-cover image classification. *ISPRS J. Photogramm. Remote Sens.* **2017**, *130*, 277–293. [[CrossRef](#)]
66. Lebourgeois, V.; Dupuy, S.; Vintrou, É.; Ameline, M.; Butler, S.; Bégué, A. A Combined Random Forest and OBIA Classification Scheme for Mapping Smallholder Agriculture at Different Nomenclature Levels Using Multisource Data (Simulated Sentinel-2 Time Series, VHRS and DEM). *Remote Sens.* **2017**, *9*, 259. [[CrossRef](#)]
67. Gorelick, N. Segmentation. In Proceedings of the Earth Engine User Summit 2018, Dublin, Ireland, 12–14 June 2018.
68. Foody, G.M. Explaining the unsuitability of the kappa coefficient in the assessment and comparison of the accuracy of thematic maps obtained by image classification. *Remote Sens. Environ.* **2020**, *239*, 111630. [[CrossRef](#)]
69. The Australian Government Department of Sustainability, Environment, Water, Population and Communities. Available online: <https://www.dccew.gov.au/sites/default/files/documents/ssr195.pdf> (accessed on 15 May 2024).
70. Singh, P.; Singh, N.; Singh, K.K.; Singh, A. Chapter 5—Diagnosing of disease using machine learning. In *Machine Learning and the Internet of Medical Things in Healthcare*; Singh, K.K., Elhoseny, M., Singh, A., Elngar, A.A., Eds.; Academic Press: Cambridge, MA, USA, 2021; pp. 89–111.
71. W&B Fully Connected. Available online: <https://wandb.ai/mostafaibrahim17/ml-articles/reports/An-Introduction-to-the-F1-Score-in-Machine-Learning--Vmlldzo2OTY0Mzg1> (accessed on 25 May 2024).
72. Open Library. Available online: <https://ecampusontario.pressbooks.pub/remotesensing/chapter/chapter-7-accuracy-assessment/> (accessed on 25 May 2024).
73. Fernández-Guisuraga, J.M.; Fernandes, P.M.; Marcos, E.; Beltrán-Marcos, D.; Sarricolea, P.; Farris, M.; Calvo, L. Caution is needed across Mediterranean ecosystems when interpreting wall-to-wall fire severity estimates based on spectral indices. *For. Ecol. Manag.* **2023**, *546*, 121383. [[CrossRef](#)]
74. Key, C.; Benson, N. Landscape Assessment (LA) Sampling and Analysis Methods. In *FIREMON: Fire Effects Monitoring and Inventory System*; Lutes, D.C., Ed.; U.S. Department of Agriculture, Forest Service, Rocky Mountain Research Station: Fort Collins, CO, USA, 2006; p. 55.
75. Çömert, R.; Matcı, D.K.; Avdan, U. Object based burned area mapping with random forest algorithm. *Int. J. Eng. Geosci.* **2019**, *4*, 78. [[CrossRef](#)]
76. Fernández-Guisuraga, J.M.; Fernandes, P.M.; Tárrega, R.; Beltrán-Marcos, D.; Calvo, L. Vegetation recovery drivers at short-term after fire are plant community-dependent in mediterranean burned landscapes. *For. Ecol. Manag.* **2023**, *539*, 121034. [[CrossRef](#)]

77. García-Redondo, C.; Díaz-Raviña, M.; Regos, A. Long-Term Cumulative Effects of Wildfires on Soil-Vegetation Dynamics in the “Baixa Limia–Serra do Xurés” Natural Park. *Span. J. Soil Sci.* **2024**, *14*, 13103. [[CrossRef](#)]
78. Jimeno-Llorente, L.; Marcos, E.; Fernández-Guisuraga, J.M. The Effects of Fire Severity on Vegetation Structural Complexity Assessed Using SAR Data Are Modulated by Plant Community Types in Mediterranean Fire-Prone Ecosystems. *Fire* **2023**, *4*, 450. [[CrossRef](#)]
79. The Australian Government Department of Agriculture, Water and the Environment. Available online: <https://www.dceew.gov.au/sites/default/files/documents/ktp-fire-regimes-that-cause-declines-in-biodiversity-advice.pdf> (accessed on 21 October 2024).
80. Nasiri, V.; Hawryło, P.; Janiec, P.; Socha, J. Comparing Object-Based and Pixel-Based Machine Learning Models for Tree-Cutting Detection with PlanetScope Satellite Images: Exploring Model Generalization. *Int. J. Appl. Earth Obs. Geoinf.* **2023**, *125*, 103555. [[CrossRef](#)]
81. Feng, C.; Zhang, W.; Deng, H.; Dong, L.; Zhang, H.; Tang, L.; Zheng, Y.; Zhao, Z. A Combination of OBIA and Random Forest Based on Visible UAV Remote Sensing for Accurately Extracted Information about Weeds in Areas with Different Weed Densities in Farmland. *Remote Sens.* **2023**, *15*, 4696. [[CrossRef](#)]
82. Thomasberger, A.; Nielsen, M.M.; Flindt, M.R.; Pawar, S.; Svane, N. Comparative Assessment of Five Machine Learning Algorithms for Supervised ObjectBased Classification of Submerged Seagrass Beds Using High-Resolution UAS Imagery. *Remote Sens.* **2023**, *15*, 3600. [[CrossRef](#)]
83. Varma MK, S.; Rao NK, K.; Raju, K.K.; Varma GP, S. Pixel-Based Classification Using Support Vector Machine Classifier. In Proceedings of the 2016 IEEE 6th International Conference on Advanced Computing, Bhimavaram, India, 27–28 February 2016.

Disclaimer/Publisher’s Note: The statements, opinions and data contained in all publications are solely those of the individual author(s) and contributor(s) and not of MDPI and/or the editor(s). MDPI and/or the editor(s) disclaim responsibility for any injury to people or property resulting from any ideas, methods, instructions or products referred to in the content.